

Improved Delayed Detached Eddy Simulation of Supersonic Combustion Fueled by Liquid Kerosene

Wubingyi Shen¹, Yue Huang^{1,*}, Wei Yao^{2,3,*}, Hedong Liu⁴, Yancheng You¹

¹*School of Aerospace Engineering, Xiamen University, Xiamen, 361005, China*

²*Key Laboratory of High-Temperature Gas Dynamics, Institute of Mechanics, Chinese Academy of Science, Beijing 100190, China*

³*School of Engineering Science, University of Chinese Academy of Science, Beijing 100049, China*

⁴*Institute of Artificial Intelligence, Xiamen University, Xiamen, 361005, China*

*Corresponding author: Yue Huang, huangyue@xmu.edu.cn; Wei Yao, weiyao@imech.ac.cn

Abstract

The purpose of this study is to quantitatively investigate the influence of diffusion characteristics and equivalence ratio (ER) of gaseous/liquid kerosene on transient combustions in a three-dimensional cavity-based scramjet combustor using Improved Delayed Detached Eddy Simulation (IDDES) with a 19 species and 54 reactions kerosene/air mechanism. Additionally, the similarities and differences between gaseous and liquid kerosene supersonic combustion are identified based on the analysis of characteristics, such as pressure, mixture fraction, temperature, and heat release rate distributions. The findings indicated that the injection velocity of liquid kerosene is an order of magnitude lower than that of gaseous kerosene; however, the residence time of liquid kerosene in the cavity was amplified by two orders of magnitude. The results also highlighted the substantial differences in the reaction heat release position between gaseous and liquid kerosene combustion. For a combustion process of liquid kerosene at an ER of 0.215, there is no obvious boundary layer separation in the isolator. The combustion process is controlled by the mixing efficiency of the shear layer, and the mode of combustion is cavity shear-layer stabilized combustion. However, when the ERs are 0.27 and 0.43, the flame propagates upstream of the cavity and forms boundary layer separation and oblique shock waves. The combustion process is now controlled by the fuel transportation in the cavity recirculation zone, and the mode of combustion is the cavity recirculation-zone stabilized combustion.

Keywords: Improved Delayed Detached Eddy Simulation; Liquid Kerosene; Skeletal Reaction Mechanism; Equivalence Ratio; Cavity-based Scramjet Combustor; Supersonic Combustion

39 Nomenclature

A	Droplet surface area
C_p	Specific heat
Da	Damköhler number
D_α	Average species α diffusion rate
d_w	Distance to wall
D_T	Average thermal diffusion rate
D_ξ	Mixture diffusivity
e_0	Specific stagnation internal energy
G_f	Drop flash vaporization rate
h	Specific static enthalpy
h_0	Specific stagnation enthalpy
h_{\max}	Grid largest length scale
h_{wn}	Length scale in wall-perpendicular direction
Ka	Karlovitz number
k_{res}	Turbulent kinetic energy of the resolved motions
k_t	Unresolved turbulent kinetic energy
\dot{m}_f	Total kerosene mass flow rate
$\dot{m}_{f,mix}$	Mixed kerosene mass flow rate
\dot{m}_p	Volumetric phase change rate
$\langle \dot{m}_p \rangle_{zone}$	Zone-average phase change rate
p	Static pressure
$P(\eta)$	Instantaneous mixture fraction
Pr_t	Turbulent Prandtl number

Q_α	Characterization mass fraction
Q'_α	Local zone mean pulsation
q_j	Heat flux vector
S_{ij}	Strain rate
Sc_t	Turbulent Schmidt number
T_b	Particle temperature
T_L	Local boiling temperature
\bar{T}_t	Local total temperature
$T_{t,\infty}$	Inlet total temperature
$T_{t,ideal}$	Ideal total temperature
u_i	Velocity component of direction
\vec{U}	Velocity vector
ν	Kinematic viscosity coefficient
$V_{\alpha,j}$	Diffusion velocity for species
ν_{sgs}	Turbulent viscosity
W	Chemical reaction rate
x_i	Coordinates of i in the x-direction of the Cartesian coordinate system
Y_α	Instantaneous mass fraction
Y'_α	Conditional mean pulsation of the instantaneous mass fraction
$Y_{l,\alpha}$	Mass fraction of species α in the liquid phase

40

41 **Greek symbols**

α_{mix}	Mass fraction of mixed kerosene
α_s	Overall heat transfer coefficient

α_{st}	Kerosene stoichiometric mass fraction
χ	Scalar dissipation rate
δ_{ij}	Kronecker delta
ε	Turbulence dissipation rate
η	Sampling variable in the mixed fractional space
η_c	Combustion efficiency
η_{mix}	Mixing efficiency
μ_l	Molecular viscosity
ρ	Density
ξ	Instantaneous mixture fraction
ξ_l	Liquid composition expressed in mixture fraction
$\bar{\omega}_\alpha$	Average mass production rate of chemical species α
τ_c	Chemical time scale
τ_{ij}	Strain rate tensor
τ_k	Kolmogorov time scales
τ_t	Taylor time scale
$\tilde{\nu}$	Kinematic eddy viscosity
$\Psi_{\alpha,j}$	Turbulent species diffusion flux
Δ_{grid}	Subgrid length scale

1. Introduction

Compared with hydrogen, hydrocarbons are more practical fuels for scramjet operating in for lower hypersonic flight regime (Mach number < 8) [1, 2]. As a common fossil fuel, liquid kerosene is a desirable fuel for scramjets due to its high volumetric energy density among hydrocarbons and ease of handling. During the last two decades, experimental studies were conducted to investigate

the feasibility of kerosene as a scramjet fuel through examining its characteristics of ignition [3-5], flame stabilization[5-7] and propagation[8, 9]. The influences of different designs of fuel injectors[3, 4], pilot flame[7, 8], and cavity flameholders[6, 7, 10-13] are compared based on the measurements of wall pressure, wall heat flux, fluorescence and chemiluminescence intensity.

Although plenty of experimental studies have been conducted to investigate the combustion characteristics of liquid kerosene in scramjet[7, 14, 15], knowledge on the mixing, ignition, and combustion process inside the combustor is still limited due to the difficulty in diagnosing supersonic internal flow. For this, computational fluid dynamic (CFD) has been frequently applied to understand the internal flow characteristics of supersonic combustion[16, 17]. However, for supersonic combustion based on liquid kerosene, both experimental diagnosis and numerical modeling are especially difficult, as two phases are involved and interact with the shock waves, turbulence, and combustion during the droplet breakage and vaporization. The chemistry is also much more complex for hydrocarbons than hydrogen, resulting in huge computational cost that scales with the power of species number. To alleviate the modeling cost of liquid kerosene combustion, most of the previous modeling studies use gaseous surrogates[10, 18] and global mechanisms[2, 19-22], which assume that liquid kerosene has been completely vaporized before combustion and the chemistry reaches equilibrium immediately after ignition. However, the rapid vaporization and fast chemistry predict a more concentrated heat release, unphysical thermal choking[23], and higher peak pressure with errors up to 35-56%[21]. Compared with detailed chemistry, the global mechanism cannot accurately reproduce the auto-ignition and progressive burning[24], which are important to describe the kerosene combustion with a comparable chemical time scale to the residence time of supersonic flow.

In addition to the simplifications of gaseous kerosene and global mechanism, Reynolds-averaged Navier–Stokes (RANS) modeling is frequently applied to kerosene modeling[20, 25-29] as it requires lower computation cost. However, large unsteadiness exists in the supersonic combustion field of kerosene since the time scale ranges of supersonic flow, chemistry, and evaporation overlap. Ignorance of the influence of fluctuations on mixing and chemical reactions will lead to erroneous predictions on combustion performance.

High-fidelity Large Eddy Simulation (LES)[30] that directly resolves unsteady flow motions were employed for gaseous kerosene and revealed important unsteady mixing and combustion characteristics. LES could capture dynamic combustion characteristics more accurately. However, LES simulation that incorporate skeletal mechanisms and gas-liquid phase transition is difficult to accept due to limited computing resources. High-resolution LES modeling that incorporate skeletal mechanisms are scarce in the literature for liquid kerosene. Accurate descriptions of the vaporization of liquid droplets into gaseous kerosene and the pyrolysis of kerosene into smaller hydrocarbons are especially important to reproduce the combustion behavior in a scramjet, as their slow process relative to the supersonic crossflow will typically cause a delayed ignition and a further downstream flame stabilization[21, 31, 32]. In order to balance the calculation cost and capture the accuracy of reaction characteristics, IDDES is selected for numerical simulation

To gain an in-depth understanding of the characteristics of supersonic combustion fueled by liquid kerosene, a high-resolution Improved Delayed Detached Eddy Simulation (IDDES) with high-fidelity physical and chemical models is conducted in this study. The combustion chemistry is based on a skeletal mechanism with 19 species and 54 reactions[18]. Section 2 introduces the two-phase Euler-Lagrange framework for the transport and evaporation of liquid kerosene droplets.

Section 3 describes the modeling of turbulence-chemistry interaction via Dynamic Zone Flamelet Model (DZFM) and hybrid RANS/LES approach. The combustion modeling based on gaseous and liquid kerosene under the same equivalence ratio is investigated as well.

2. Numerical methods and setup

2.1. Computational approach

2.1.1. Governing equations and IDDES model

The numerical simulation is based on the unsteady three-dimensional compressible Navier–Stokes equation, and the continuity equation is as follows:

$$\frac{\partial \rho}{\partial t} + \frac{\partial \rho u_i}{\partial x_j} = 0 \quad (1)$$

where u_i and ρ are the velocity components of direction and pressure, respectively.

The momentum equation is defined as:

$$\frac{\partial \rho u_i}{\partial t} + \frac{\partial \rho u_i u_j}{\partial x_j} = -\frac{\partial p}{\partial x_i} + \frac{\partial \tau_{ij}}{\partial x_j} \quad (2)$$

where τ_{ij} is the viscous stress tensor, , expressed as:

$$\tau_{ij} = 2\mu_l \left(S_{ij} - \frac{1}{3} \frac{\partial u_k}{\partial x_k} \delta_{ij} \right) \quad (3)$$

where μ_l is the molecular viscosity and δ_{ij} is the Kronecker delta. The strain rate is defined as:

$$S_{ij} = \frac{1}{2} \left(\frac{\partial u_i}{\partial x_j} + \frac{\partial u_j}{\partial x_i} \right) \quad (4)$$

The energy equation is given by:

$$\frac{\partial \rho e_0}{\partial t} + \frac{\partial \rho u_j h_0}{\partial x_j} = -\frac{\partial q_j}{\partial x_j} + \frac{\partial \tau_{ij} u_i}{\partial x_j} \quad (5)$$

where q_j is the heat flux vector. The specific stagnation internal energy e_0 and specific

stagnation enthalpy, h_0 , are defined as:

$$e_0 = h - \frac{p}{\rho} + \frac{1}{2} u_i u_i \quad (6)$$

$$h_0 = e_0 + \frac{p}{\rho} \quad (7)$$

The species transport equation is defined using the species mass fraction:

$$\frac{\partial \rho Y_\alpha}{\partial t} + \frac{\partial \rho u_j Y_\alpha}{\partial x_j} = \dot{\omega}_\alpha - \frac{\partial \rho V_{\alpha,j} Y_\alpha}{\partial x_j}, \alpha = 1, \dots, N_s - 1 \quad (8)$$

where Y_α is the reaction rate for species α . $V_{\alpha,j}$ is the j component of the diffusion velocity for species α .

The IDDES model used in the present study is based on the one equation Spalart–Allmaras (SA) turbulence model[33]. The turbulent viscosity is computed by the Spalart–Allmaras one equation model, which solves a transport equation for the kinematic eddy viscosity $\tilde{\nu}$.

$$\frac{D(\rho \tilde{\nu})}{Dt} = c_{b1} \tilde{S} \rho \tilde{\nu} - c_{w1} f_w \rho \left(\frac{\tilde{\nu}}{d} \right)^2 + \frac{\rho}{\sigma} \left\{ \nabla [\nu + \tilde{\nu}] \nabla \tilde{\nu} + c_{b2} (\nabla \tilde{\nu})^2 \right\} \quad (9)$$

$$\tilde{S} = S + \frac{\tilde{\nu}}{\text{Re}_\infty \kappa^2 l_{hyb}^2} f_{v2}, f_{v2} = 1 - \frac{\chi}{1 + \chi f_{v1}} \quad (10)$$

$$f_{v1} = \frac{\chi}{\chi + c_{v1}^3}, \chi = \frac{\tilde{\nu}}{\nu}, f_w = g \left[\frac{(1 + c_{w3}^6)}{(g^6 + c_{w3}^6)} \right]^{1/6} \quad (11)$$

$$g = r + c_{w2}(r^6 - r), r = \frac{\tilde{\nu}}{\text{Re}_\infty \tilde{S} \kappa^2 d^2} \quad (12)$$

The equations for LES can be obtained by applying a filter to the instantaneous governing equations. Although Favre filtering is conceptually different to the Favre averaging process and the resulting system of equations has a different physical meaning, they are visually identical to the RANS equations. The only modification required is the way in which the turbulent viscosity is calculated, and more details can be seen in our previous work[34]. In IDDES, the subgrid length

scale[35] is used by

$$\Delta_{grid} = \min\{\max[C_w d_w, C_w h_{\max}, h_{wn}], h_{\max}\} \quad (13)$$

where d_w and h_{\max} is distance to wall and the grid largest length scale. h_{wn} is the length scale in wall-perpendicular direction and the coefficient $C_w = 0.15$. The LES model is closed by the Spalart-Allmaras one equation model through setting the length scale as $C_{DES} \Delta_{grid}$ in the LES region, where $C_{DES} = 0.65$. IDDES hybrid turbulent length scale[35] is given as:

$$L_{IDDES} = \tilde{f}_d (1 + \tilde{f}_e) L_{RANS} + (1 - \tilde{f}_d) L_{LES} \quad (14)$$

$$L_{RANS} = d_w, L_{LES} = C_{DES} \Delta_{grid} \quad (15)$$

Blending functions \tilde{f}_d and \tilde{f}_e are given as:

$$\tilde{f}_d = \max\{(1 - f_{dt}), f_B\} \quad (16)$$

$$f_{dt} = 1 - \tanh[(8r_{dt})^3] \quad (17)$$

$$r_{dt} = \frac{V_t}{k^2 d_w^2 \max\{[\sum_{ij} (\partial u_i / \partial x_j)^2]^{0.5}, 10^{-10}\}} \quad (18)$$

$$f_B = \min\{2 \exp(-9\alpha^2), 1.0\}, \alpha = 0.25 - d_w / h_{\max} \quad (19)$$

The model constants are:

κ	c_{b1}	c_{b2}	c_{w2}	c_{w3}	σ	c_{v1}
0.41	0.1355	0.622	0.3	2.0	0.6667	7.1

2.1.2. Combustion model

The combustion model used in this study is the dynamic zone flamelet model[36]. The flamelet variable is defined as the conditional mean over a zone:

$$Q_\alpha = \langle Y_\alpha | \xi(x, t) = \eta, x \in zone \rangle \quad (20)$$

where η is the sampling variable in the mixed fractional space, subscript *zone* indicates the

conditional average within the zone and ξ represents the instantaneous mixture fraction.

The relation between instantaneous mass fraction Y_α and conditionally averaged mass fraction

Q_α is as follows:

$$Y_\alpha(x, t) = Q_\alpha(\eta = \xi(x, t), x \in zone, t) + Y'_\alpha(x \in zone, t) \quad (21)$$

Y'_α represents the fluctuation of the instantaneous value deviating from Q_α . Since the conditional

average of $Q'_\alpha = \langle Y'_\alpha | \eta, x \in zone \rangle = 0$, the mean mixture fraction can be obtained as follows:

$$\tilde{Y}_\alpha = \frac{1}{\rho_\eta} \int \rho_\eta Q_\alpha p(\eta) d\eta \quad (22)$$

in which $P(\eta)$ is the probability density function (PDF) describing the instantaneous mixture

fraction, and $\rho_\eta = \langle \rho | \eta, x \in zone \rangle$ is the zone conditional average of density. Through refining

and dynamically updating the zone division based on multiple flow variable indices, e.g., mixture

fraction, temperature, pressure, and reaction progressive variable, a local statistically homogeneity

of conditional variables can be assumed, i.e., their spatial terms in physical space can be ignored

within the zone, and the fluctuation is considered to be small $\tilde{Y}_\alpha \rightarrow 0$.

The instantaneous equations for mass, mixture fraction, and species considering phase

exchange are as follows:

$$\frac{\partial \rho}{\partial t} + \nabla \cdot (\rho \vec{U}) = \dot{m}_p \quad (23)$$

$$\frac{\partial \rho \xi}{\partial t} + \nabla \cdot (\rho \vec{U} \xi) = \left(\rho \frac{\partial \xi}{\partial t} + \rho \vec{U} \cdot \nabla \xi \right) + \xi \left(\frac{\partial \rho}{\partial t} + \nabla \cdot (\rho \vec{U}) \right) - \nabla \cdot (\rho D_\xi \nabla \xi) = \dot{m}_p \xi \quad (24)$$

$$\frac{\partial \rho Y_\alpha}{\partial t} + \nabla \cdot (\rho \vec{U} Y_\alpha) = \left(\rho \frac{\partial Y_\alpha}{\partial t} + \rho \vec{U} \cdot \nabla Y_\alpha \right) + Y_\alpha \left(\frac{\partial \rho}{\partial t} + \nabla \cdot (\rho \vec{U}) \right) - \nabla \cdot (\rho D_\alpha \nabla Y_\alpha) = \dot{m}_p Y_{l,\alpha} + \rho W_\alpha \quad (25)$$

\vec{U} is the velocity vector, D_α is the diffusivity of species α , D_ξ is the mixture diffusivity, and

W represents the chemical reaction rate. \dot{m}_p is the volumetric phase change rate, $Y_{l,\alpha}$ is the

mass fraction of species α in the liquid phase, ξ_l is the liquid composition expressed in mixture

fraction given by $\xi_l = \sum Y_{l,\alpha}$ with species α corresponding to the fuel species.

Differentiating Eq. (21), substituting it in Eq. (25), and then combining with Eq. (23) and (24),

the final conditional equation that incorporates the phase change effect can be written as:

$$\begin{aligned} \rho_\eta \frac{\partial Q_\alpha}{\partial t} + \langle \rho \vec{U} | \eta \rangle_{zone} \cdot \nabla Q_\alpha + \langle \dot{m}_p \rangle_{zone} (Q_\alpha - Y_{l,\alpha} + \frac{\partial Q_\alpha}{\partial \eta} (\xi_l - \eta)) = \\ \rho_\eta \frac{D_\alpha}{D_\xi} \langle \chi | \eta \rangle_{zone} \frac{\partial^2 Q_\alpha}{\partial \eta^2} + \rho_\eta \left(\frac{D_\alpha}{D_\xi} - 1 \right) M_\eta \frac{\partial Q_\alpha}{\partial \eta} + \rho_\eta \langle W_\alpha | \eta \rangle \end{aligned} \quad (26)$$

where the third term on the left-hand side represents the contribution from the phase exchange,

$\langle \dot{m}_p \rangle_{zone}$ is the zone-average phase change rate. For pure liquid droplets, it has a value of $\xi_l = 1$.

The scalar dissipation rate is modeled using the amplitude mapping closure model[37].

Conditional temperature and conditional diffusion are obtained from a historical statistic method

[37].

2.1.3. Liquid phase model

The Euler-Lagrangian approach is used to model the liquid kerosene jet, whose breaking is rapid in supersonic flow. Two-way interaction is modeled through coupling the source terms of Lagrangian droplets and flow field for mass, momentum, species, enthalpy, and radiation. The volume of Lagrangian droplets is assumed to be constant before the complete evaporation. The distorted sphere drag model[38] is used to simulate the force acting on the droplets. Stochastic dispersion Reynolds Averaged Simulation model[39] is used to simulate the turbulence dispersion effect. The Kelvin-Helmholtz Rayleigh-Taylor[40] model is used to simulate the jet breakup. Phase change is simulated by the liquid evaluation boil model[41], where the droplet flash vaporization rate G_f is given as:

$$G_f = \frac{\alpha_s (T_p - T_b) A}{L(T_b)} \quad (27)$$

In Eq. (27), A is the droplet surface area, T_b is the particle temperature, and T_L is the local boiling temperature. α_s is an overall heat transfer coefficient from the droplet interior to the droplet surface correlated as:

$$\alpha_s = \begin{cases} 0.76(T_L - T_b)^{0.26} & 0 \leq T_L - T_b \leq 5 \\ 0.027(T_L - T_b)^{2.33} & 5 \leq T_L - T_b \leq 25 \\ 13.8(T_L - T_b)^{0.39} & 25 \leq T_L - T_b \end{cases} \quad (28)$$

Based on the analysis by Ran Marshall[42], the local interaction model is adopted for the wall treatment method. The inlet, outlet, and kerosene injection inlet are set as the escape boundary, while all other walls are set as rebound walls.

2.1.4. Chemical reaction mechanism

Kerosene is surrogated by a three-component model composed of 28.8 % iso-octane, 62.4 % n-decane, and 8.8 % n-propyl cyclohexane. The modeling parameters for liquid kerosene injection are listed in Table 1. The skeletal mechanism for kerosene pyrolysis and combustion consists of 19 species and 54 reactions, which have been extensively validated under scramjet conditions [43]. To speed up the solving of stiff chemistry, Zonal Dynamic Adaptive Chemistry (Z-DAC) and Zonal In Situ Adaptive Tabulation (Z-ISAT) are used [44]. Both Z-DAC and Z-ISAT firstly partition the flow field dynamically according to the local thermo-chemical state parameters, such as mixture fraction, temperature, pressure, and reaction progress variables, and then reduce different subset mechanisms and build separate ISAT tables for each zone. Since the thermo-chemical state of each zone is relatively stable and homogeneous, such zone-based DAC mechanism and ISAT table can be more targetable and remain valid for a long time.

212

Table 1 Kerosene injection parameters

Parameter	Value
Density (liquid) kg/m ³	728
C_p J/ (kg K)	1961
Temperature K	800
Mass Flow kg/s	0.00109
Equivalence ratio	0.43
Velocity (gas) m/s	162.32
Velocity (liquid) m/s	11.926
IC ₈ H ₁₈ mass fraction	0.288
NC ₁₀ H ₂₂ mass fraction	0.624
PCH mass fraction	0.088

213 *2.1.5. Numerical method*

214 The solver adopts the compressible density-based supersonic combustion solver Amber [44]
215 developed based on OpenFOAM framework. The nonlinear inviscid convective flux is calculated
216 by a hybrid scheme combining the second-order semi-discrete central Kurganov-Tadmor scheme
217 and a second-order central scheme [45]. A third-order spatial accuracy for primitive reconstruction
218 on unstructured mesh is realized using the scale-selective discretization scheme [46], and the time
219 integration is based on the second-order Crank-Nicholson scheme.

220 *2.2. Calculation setup*

221 The experimental case of scramjet combustor fueled by liquid kerosene was conducted by Yu
222 et al.[7]. As shown in Fig. 1. the inlet of the combustor is a rectangle of 30.5 × 30 mm, and the
223 combustor can be divided into three sections. The first section is 266 mm long with a divergent
224 angle of 1°, the second section is 300 mm long with a divergent angle of 3°, and the third section is
225 336 mm long with a divergent angle of 4°. The cavity is located 115 mm downstream of the inlet.

The cavity length is 45 mm, and the depth is 8 mm. The diameter of the fuel injection porthole is 0.4 mm, which is 5 mm away from the rear wall of the cavity.

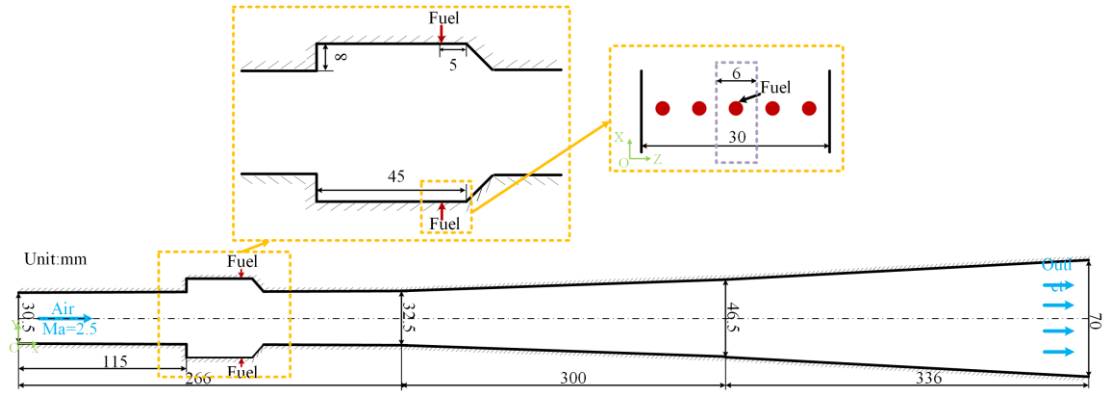


Fig. 1. Structural parameters of the combustor

Four cases configured as Table 2 were modeled to reveal the influence of equivalence ratio and the initial jet status on the supersonic combustion characteristics. The parameters for air crossflow on the inlet are shown in Table 3. The computational domain is 1/5 times the width of the combustor with periodic conditions on the lateral walls. Open boundary condition with zero gradients for all variables is applied to the outlet. The combustor walls are all set to adiabatic no-slip walls.

Table 2 Parameters of different cases

Case	Kerosene	Equivalence ratio	Total cell
Case1	Gas	0.43	26 million
Case2	Liquid	0.43	26 million
Case3	Liquid	0.27	26 million
Case4	Liquid	0.215	26 million

244

Table 3 Parameters of the combustor inlet

Parameter	Value
Static pressure bar	0.79
Total pressure bar	13.5
Temperature K	764.4
Total temperature K	1720
Mach number	2.5
Velocity m/s	1423
O ₂ mass fraction	0.2
H ₂ O mass fraction	0.134
N ₂ mass fraction	0.666

245 *2.3. Grid independence verification*

246 Fig. 2 compares the wall pressure predictions under different mesh resolutions with total cell
247 counts of 10 million (10M), 26 million (26M), 59 million (59M), and 104 million (104M). The
248 predictions by 26M, 59M, and 104M meshes are closer to the experimental measurements, while
249 the 10M prediction differs in the cavity position. Compared to the previous predictions[2, 25, 32] in
250 the literature, the current predictions of shock wave position and peak pressure agree better with the
251 experimental data. The peak pressure of gaseous kerosene combustion is significantly lower near
252 the cavity than the experimental data. All calculations were performed on a high-performance
253 computing cluster in the Para Cloud, where 128 cores (AMD EPYC 7452 2.35GHz) were used for
254 each case. Typical runtimes to form a steady flow were proximately 12-, 32-, 50- and 90-days wall-
255 clock time for cases with total cell counts of 10 million, 26 million, 59 million, and 104 million. The
256 26M result is selected for the other cases' modeling to reduce the computational cost.

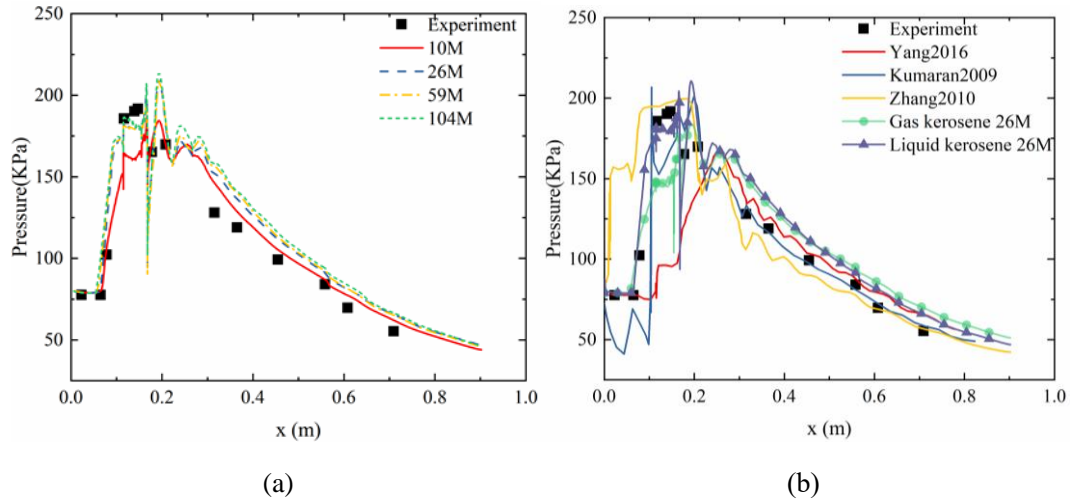


Fig. 2. Comparison of mean wall pressure a) liquid kerosene combustion with different meshes, and b) gaseous/liquid kerosene combustion compared with previous literature

3. Results and discussion

3.1 Comparison between gaseous kerosene and liquid kerosene at ER of 0.43

3.1.1 Non-reacting case

The jet penetration characteristics are especially important for the subsequent mixing and combustion. Due to the smaller density, the injection velocity of gaseous kerosene is 13 times higher than that of liquid kerosene under the same mass flow rate (see Table 1). From the mixture fraction contour in Fig. 3, the gaseous fuel jet flushes out the subsonic cavity flow directly and is less affected by the recirculation flow inside the cavity. From the streamlines in Fig. 4, the high-momentum fuel jet isolates the cavity flow on the two sides. Due to the low momentum, the penetration depth of liquid kerosene is much lower and can be easily distorted by recirculation flow. Hence, a large number of droplets are entrained into the recirculation flow and have little chance to contact the outer layer. The gathered droplets evaporate and cause a higher concentration of gaseous kerosene inside the cavity.

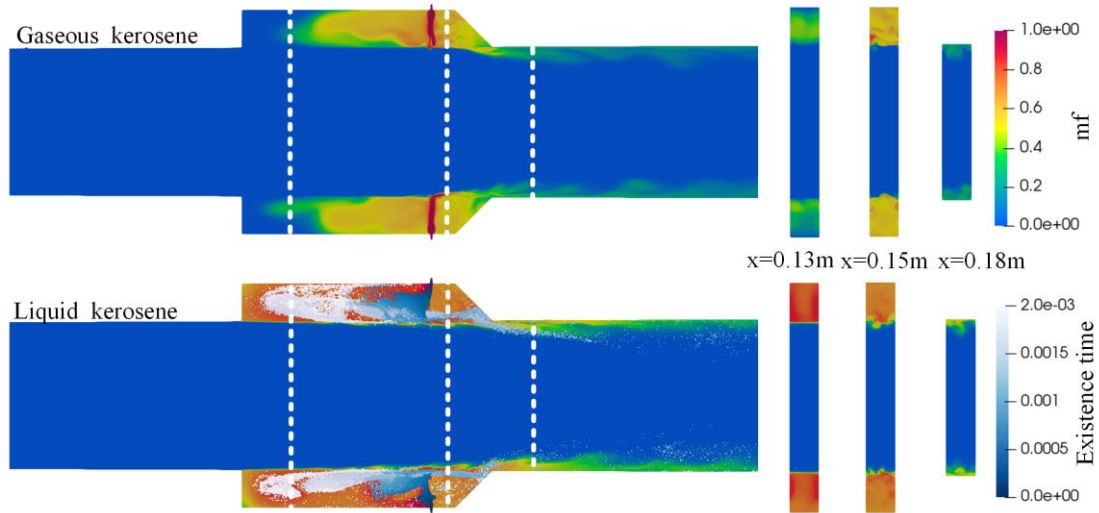


Fig.3. Mixture fraction distribution of combustor symmetry plane and cross-section along the x

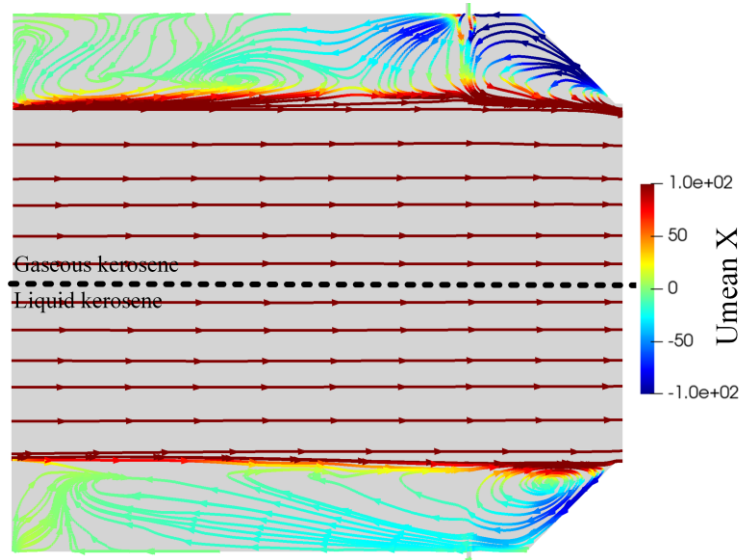


Fig. 4. Averaged streamlines colored by mean streamwise velocity for gaseous (upper) and liquid kerosene (lower)

For the convenience of analysis, the combustor is divided into six regions as labeled in Fig. 5

The existence time (ET) of kerosene droplets can be divided into three stages: 1) $ET < 1$ ms, 2) 1 ms $\leq ET \leq 1.5$ ms, and 3) 1.5 ms $< ET$. The percent of kerosene droplets in different periods of existence in each region are shown in Fig. 6. The percent of vaporized kerosene mass in each region are 0.738, 0.101, 0.101, 0, 0.015, and 0.045, respectively. Fig.7 describes the gaseous/liquid kerosene diffusion mechanism in the cold flow field. The core flow time of gaseous kerosene from

the injector is in the order of 10^{-5} s magnitude. It is less affected by the recirculation zones 1 and 2 because it directly flows into the combustor core flow. The droplet distribution of liquid kerosene is complex under the action of recirculation zone, shear layer, and combustor wall collision. The injected kerosene droplets enter Zone 2, part of which moves to Zone 3 along path 4, and the remaining move to Zone 1 along path 1 to break up and vaporize. The unvaporized kerosene droplets enter the shear layer along path 2 under the influence of recirculation-zone 1. There are many small vortexes in the shear layer and mass exchange occurs outside the cavity (path 3); hence, only a small number of kerosene droplets are present in different SMD entering Zone 5. A small number of kerosene droplets that did not participate in mass exchange and those that were initially shunted propagated downward along path 4 and collided with the rear wall of the cavity due to the influence of recirculation-zone 2. A part of the kerosene droplets after collision stays in Zone 3 along path 5 and vaporize. The remaining droplets enter Zone 6 along path 6.

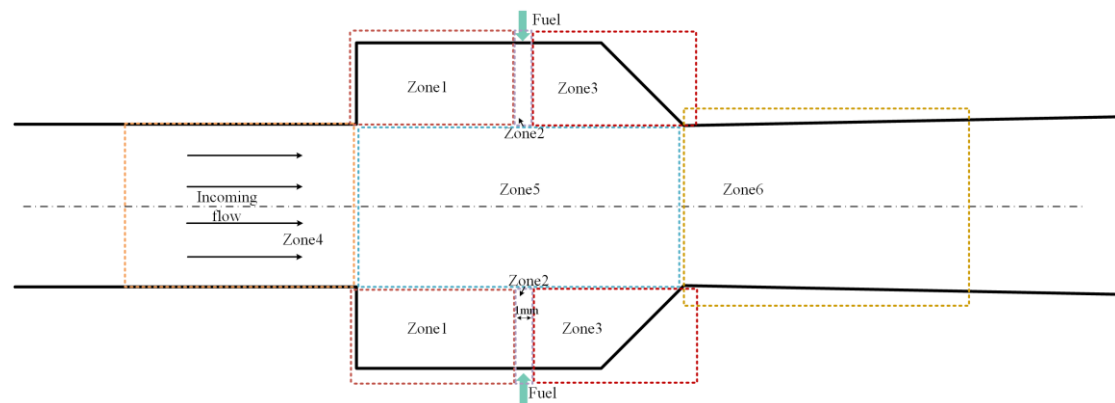


Fig. 5. Combustor division diagram

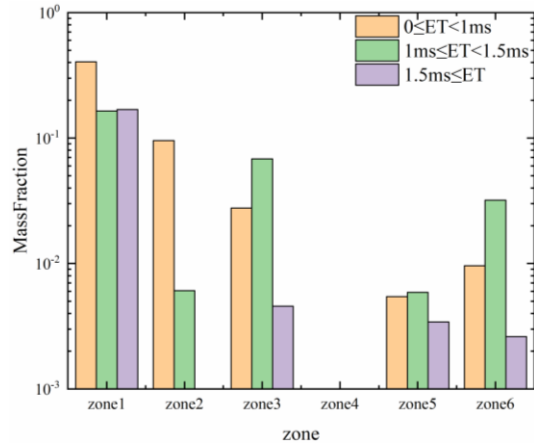
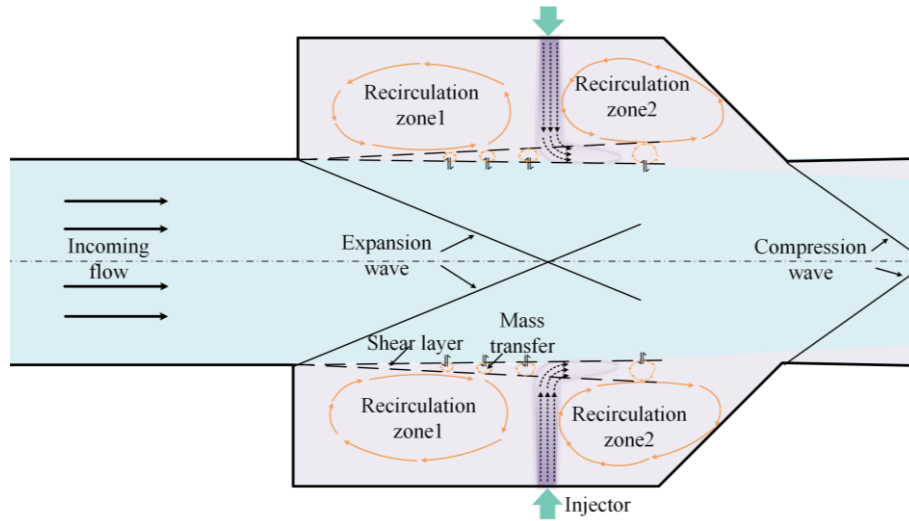
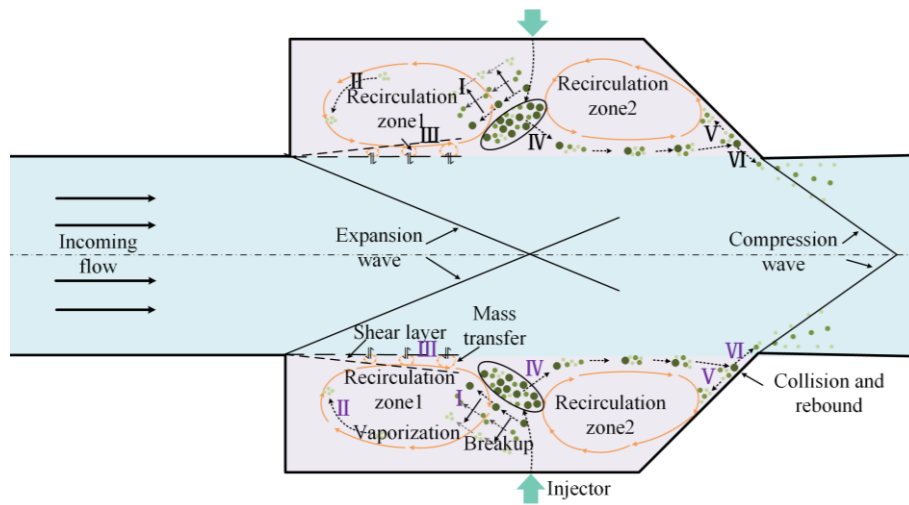


Fig. 6. Existence time (ET) distribution of kerosene droplets in six zones (liquid kerosene ER

0.43)



(a)



(b)

Fig. 7. Cold kerosene diffusion mechanism a) gaseous kerosene and b) liquid kerosene

Fig. 8 shows the total pressure recovery efficiency, mixing efficiency, and mass average Mach number of the cross-section along the x-direction. The mixing efficiency is calculated as the maximum fuel ratio that can be consumed by the available oxygen[47]. The mixing efficiency is higher for gaseous kerosene after $x = 0.16$ m because the higher penetration depth aids the momentum exchange between the fuel jet and the air crossflow. Although the liquid kerosene droplets massively accumulate in the cavity, the mixing efficiency does not show an observable rise, as the low temperature does not promote evaporation. The entrainment effect of the high-velocity gaseous jet accelerates the recirculation, and therefore the mean Mach number is higher for the gaseous kerosene case.

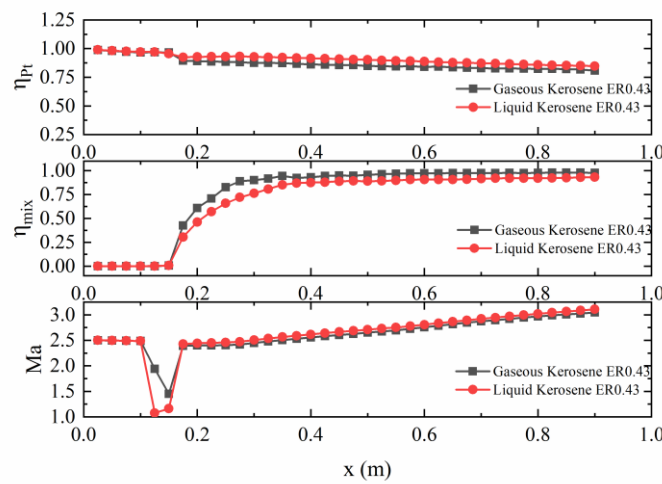
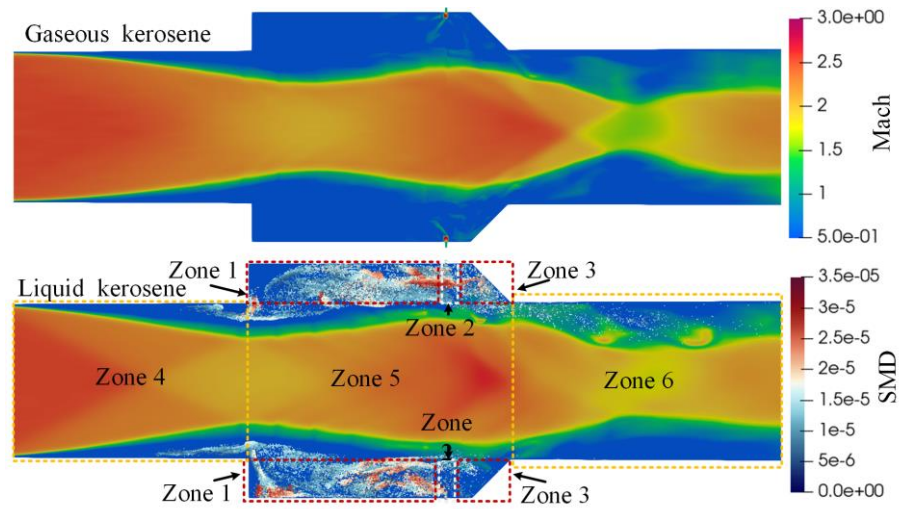


Fig. 8. Total pressure recovery efficiency, mixing efficiency, and mass average Mach number of different sections

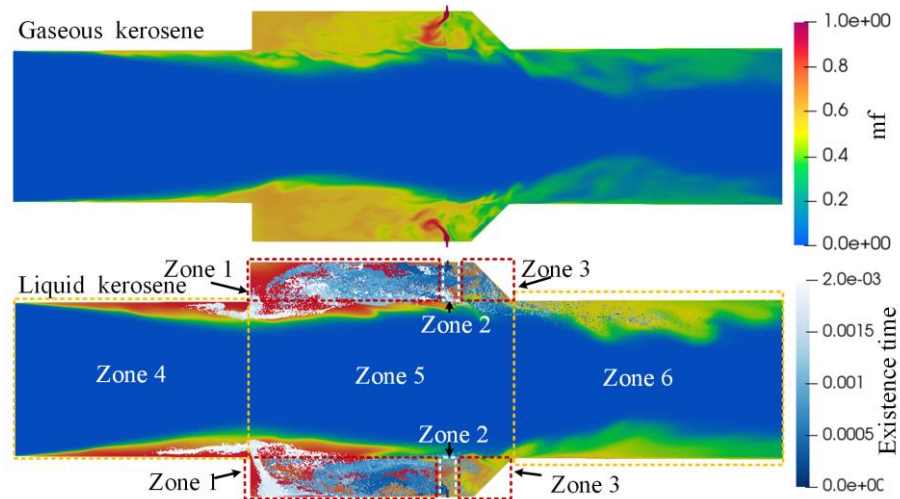
3.1.2 Reacting case

Fig. 9 shows the Mach number, mixture fraction, and kerosene particle distribution on the symmetry plane. Similar to the cold field, the mixture fraction in the cavity is lower for the gaseous kerosene case than the liquid kerosene case. Fig. 10 describes the percent of liquid kerosene droplets in each zone after injection into the cavity. The percent of kerosene droplets in each zone are 0.8863,

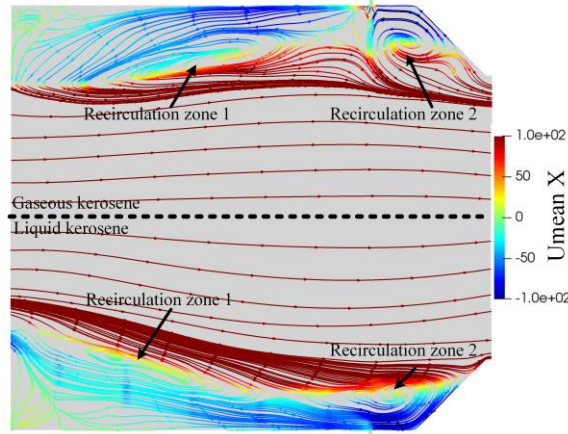
0.05, 0.0126, 0.0076, 0.03, and 0.0135, respectively. Most of the liquid kerosene particles droplets injected into the cavity move to Zone 1 due to the influence of the recirculation zone of Zone 1 (recirculation-zone 1), and some particles droplets with larger SMD are broken up during the movement.



(a)



(b)



(c)

Fig. 9. Mach number and mixture fraction distribution of combustor symmetry plane. a) Kerosene droplets color using SMD coloring, b) kerosene droplets color using existence time coloring, and c) averaged streamlines colored by mean x velocity

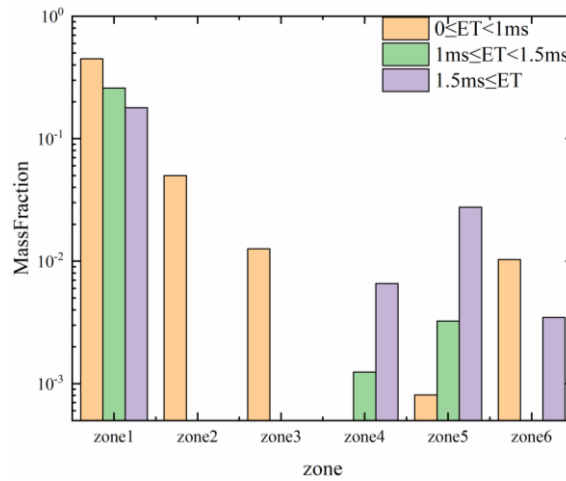
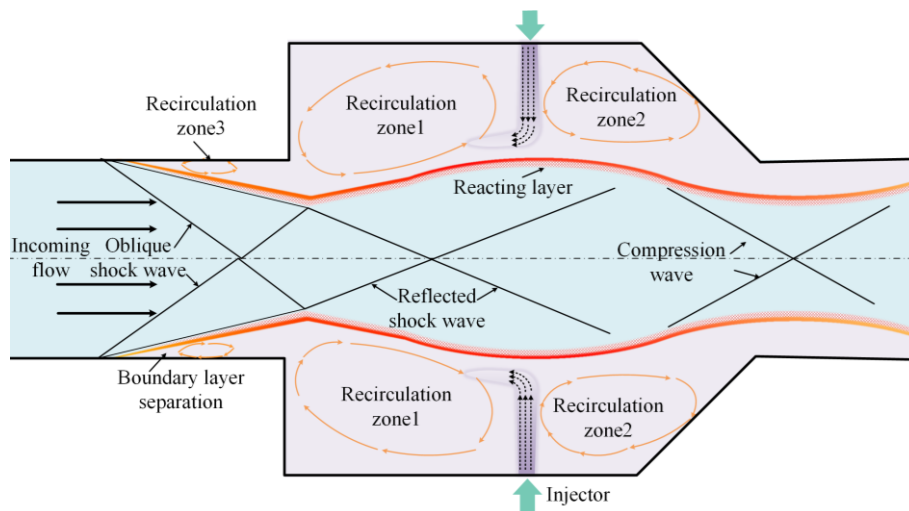


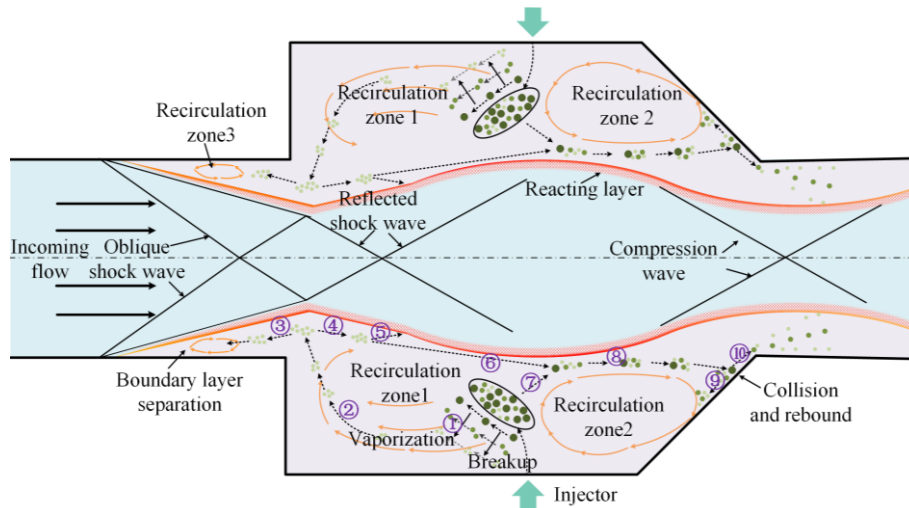
Fig. 10. Statistics of kerosene droplets in different zones ordinate is the mass fraction of kerosene droplets

Figs. 11 describes the kerosene combustion mechanism. Gaseous kerosene is injected into the cavity affected by the recirculation-zone 1, deflection diffusion, and core flow mixing reaction. Due to the increase in the heat release and backpressure of the cavity, the boundary layer is separated and oblique shock wave is formed upstream of the cavity. It is then reflected between the reacting layer, thus forming a series of reflected shock wave. The liquid kerosene droplets are the same as that in cold flow. Most of the kerosene droplets injected are broken up and vaporized along path 1,

and unvaporized kerosene droplets enter the front of the cavity along path 2 due to the influence of recirculation-zone 1. Some kerosene droplets along path 3 participate in the reaction of the boundary layer separation zone and a small number of kerosene droplets participate in the vaporization and reaction in the reaction layer of the flame. The remaining kerosene droplets propagate downstream along path 6 and converge with droplets along path 7 at the beginning. A part of the kerosene droplets after the collision is affected by the recirculation-zone 2 and vaporized along path 9 in Zone 3, while the rest enter Zone 6 along path 10 and continue to propagate downstream of the cavity. The combustion process is controlled by the kerosene transportation of the cavity recirculation zone, which can be considered as the cavity recirculation-zone stabilized combustion.



(a)



(b)

Fig. 11. Kerosene combustion mechanism a) gaseous kerosene cavity recirculation-zone stabilized combustion, b) liquid kerosene cavity recirculation-zone stabilized combustion

Fig.12 shows the numerical schlieren for the gaseous and liquid kerosene cases. Due to combustion heat release, the higher backpressure in the cavity causes the detachment of the boundary layer upstream of the cavity, forming a separation zone and oblique shock waves. The initial oblique shock wave is then reflected between the wall and the shear layer. In addition, compression waves are formed by the cavity. The foot of the initial shock wave moves more upstream for the gaseous kerosene case. From Fig.13, the temperature inside the cavity of gaseous kerosene is significantly higher than that of liquid kerosene. This is due to the absorption of latent heat during the vaporization of liquid kerosene (Fig. 14). The endothermic pyrolysis of kerosene into small hydrocarbons will also cause cold spots in the reacting field. The lower temperature inside the cavity is caused by the vaporization and pyrolysis of the concentrated liquid droplets.

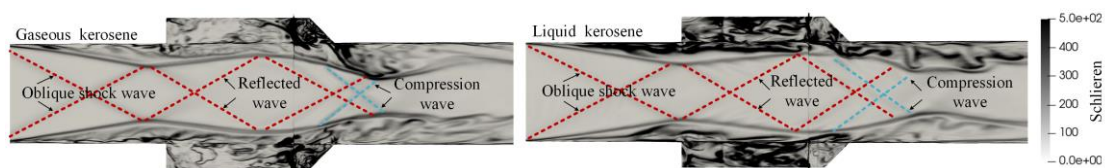


Fig. 12. Schlieren distribution of symmetry plane

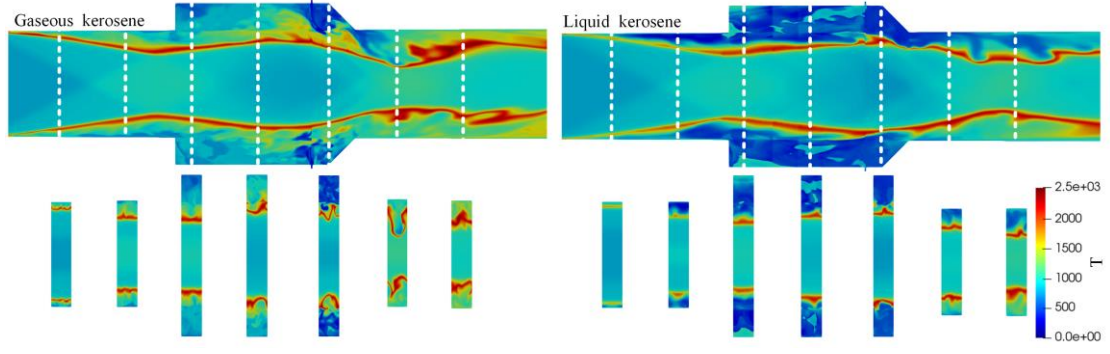


Fig. 13. Temperature distribution of combustor symmetry plane and cross-section along x-direction (line shows cross-section position along x-direction $x = 0.08, 0.1, 0.12, 0.14, 0.16, 0.18$, and 0.2 m)

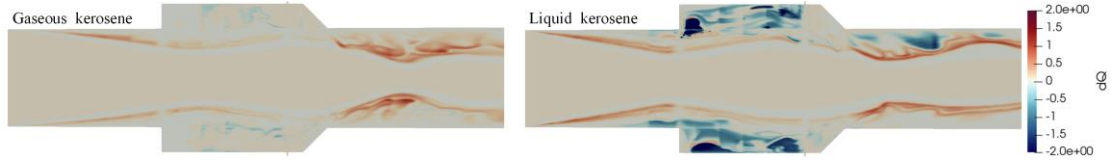


Fig. 14. Heat release rate distribution of symmetrical plane

Fig. 15 shows the combustion efficiency and mass average Mach number of the cross-section along the x-direction. Combustion efficiency η_c is defined as follows

$$\eta_c = \frac{\bar{T}_t - T_{t,\infty}}{T_{t,ideal} - T_{t,\infty}} \quad (29)$$

where \bar{T}_t , $T_{t,\infty}$ and $T_{t,ideal}$ represent local total temperature, inlet total temperature and ideal total temperature. As shown in Fig. 15, due to the vaporization process of liquid kerosene, the combustion efficiency near the cavity is lower than that of liquid kerosene. It is consistent with the phenomenon that the overall temperature in the cavity is low due to the vaporization and heat absorption of liquid kerosene which is also shown in the temperature and heat release rate distribution. The combustion of escaped kerosene droplets in the downstream of the cavity intensifies the vaporization of liquid kerosene and further strengthens the combustion.

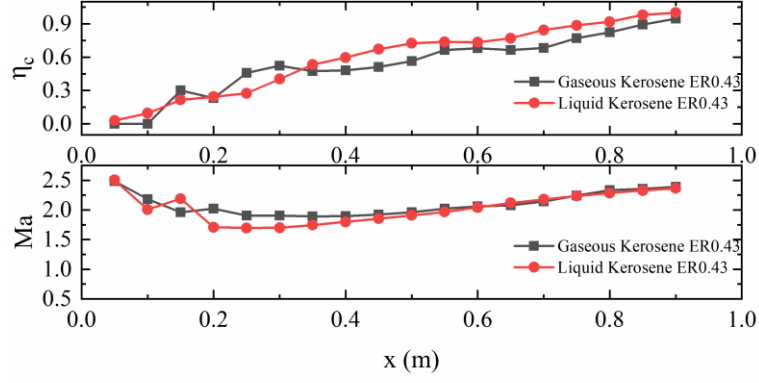


Fig. 15 Combustion efficiency, and mass average Mach number of different sections

Fig. 16 shows the turbulent chemical reaction interaction relationship of kerosene combustion in scramjet combustor based on borghi diagram. Data of borghi diagram are attached to the appendix. According to the relationship between Damköhler number, Karlovitz number, and Reynolds number. Damköhler number is defined as:

$$Da = \tau_t / \tau_c \quad (30)$$

where τ_c is the chemical time scale and Taylor time scale τ_t is defined as

$$\tau_t = (k_{res} + k_t) / \varepsilon \quad (31)$$

k_{res} is the turbulent kinetic energy of the resolved motions, k_t is the unresolved turbulent kinetic energy, and ε is turbulence dissipation rate. Karlovitz number Ka is defined as:

$$Ka = \tau_c / \tau_k \quad (32)$$

where Kolmogorov time scales $\tau_k = (\nu / \varepsilon)^{1/2}$. Reynolds number Re is defined as:

$$Re = Da^2 \cdot Ka^2 \quad (33)$$

The turbulent chemical reaction exchange is divided into the following three modes: 1) Flamelet mode: $Ka < 1, Da > 10$, 2) Thin reaction mode: $1 < Ka < 100, Da > 10$, and 3) Slow chemistry mode: $Ka > 100, Da < 10$. From the statistical analysis of the working conditions, it can be seen that most of the zones are in the flamelet mode. Historical statistics show that the percentage of the flamelet mode decreases significantly from 64.7 to 49.6% when using the liquid kerosene, whereas the percentage of the slow chemistry mode increases from 20.9 to 39.1%. This could be because the

Gaseous kerosene has stronger mixing ability; consequently, the chemical time scales increase along with the increase in Ka and decrease in Da .

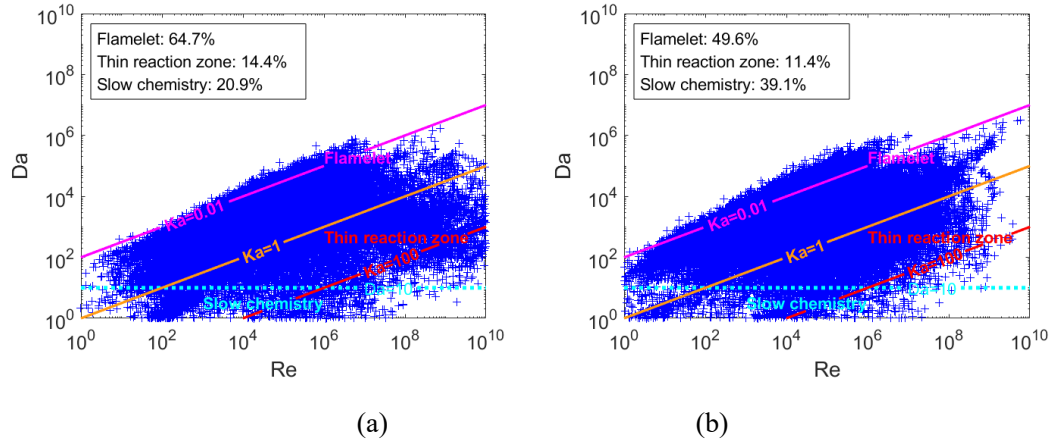


Fig. 16. Borghi diagram for a) gaseous kerosene and b) liquid kerosene combustion.

3.2 Effect of equivalence ratios

Figs. 17 and 18 show the temperature contours and numerical schlieren under two equivalence ratios (ERs). The flame is stabilized in the cavity for $ER=0.215$. The unvaporized kerosene droplets gradually fill the whole cavity, then spill out and propagate downstream along the combustor wall. The combustion is dominated by the mixing inside the shear/mixing layer along the droplet trajectory (see Figs. 19, 20) and can be considered as the cavity shear-layer stabilized mode[48]. For $ER=0.27$, the combustion is controlled by the evaporation of kerosene in the cavity recirculation zone (see Figs. 19, 20) and can be considered as the cavity recirculation-zone stabilized combustion[48]. The boundary separation position oscillates forward and backward in accordance with the periodic heat addition in the cavity.

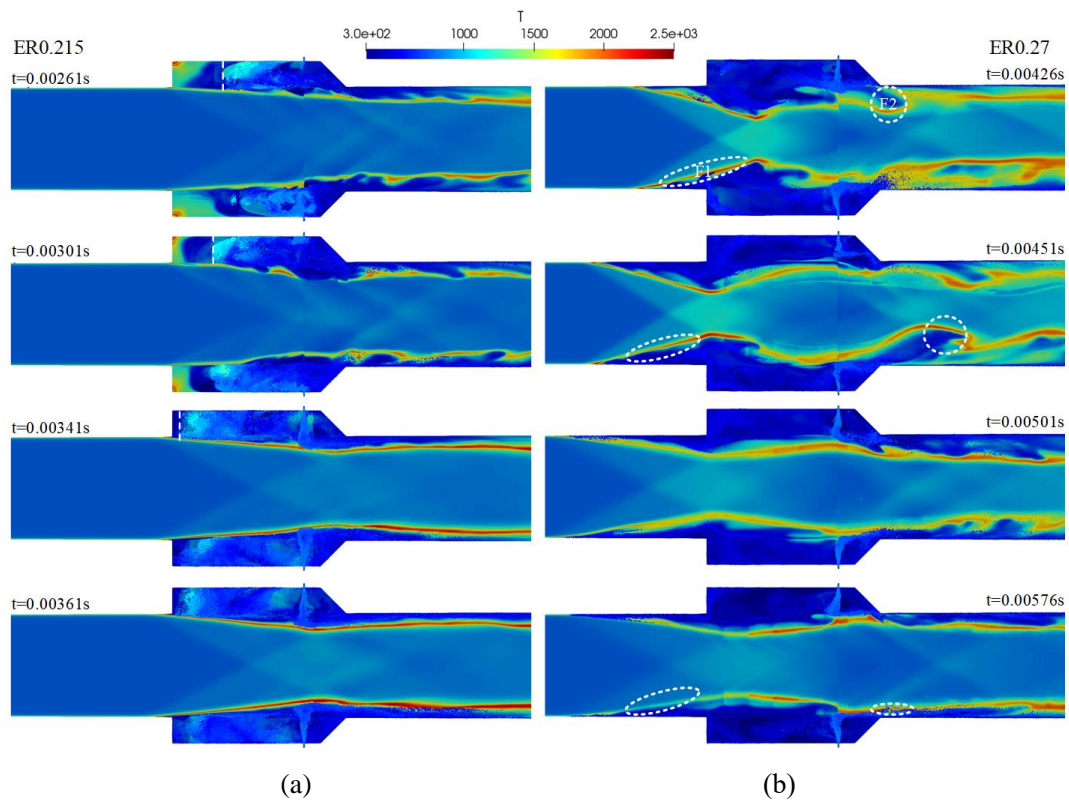


Fig. 17. Temperature distribution of liquid kerosene, a) ER 0.215 and b) 0.27

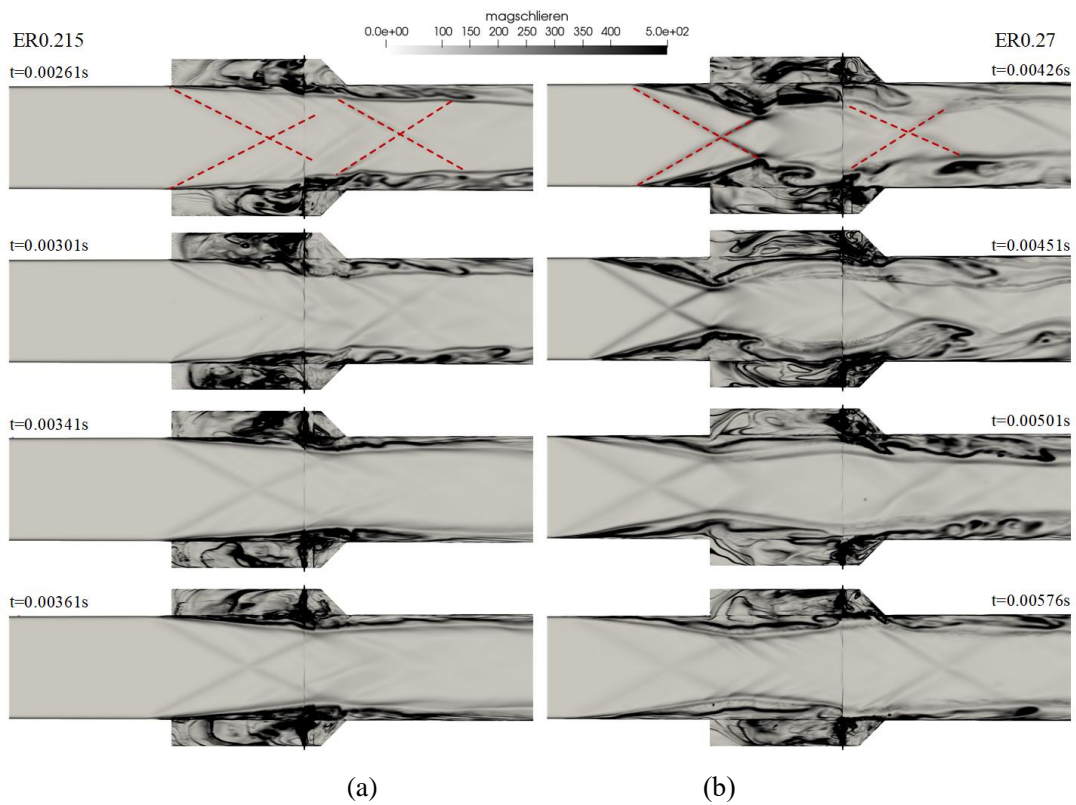


Fig. 18. Schlieren of symmetry plane a) liquid kerosene, ER 0.215, and b) 0.27

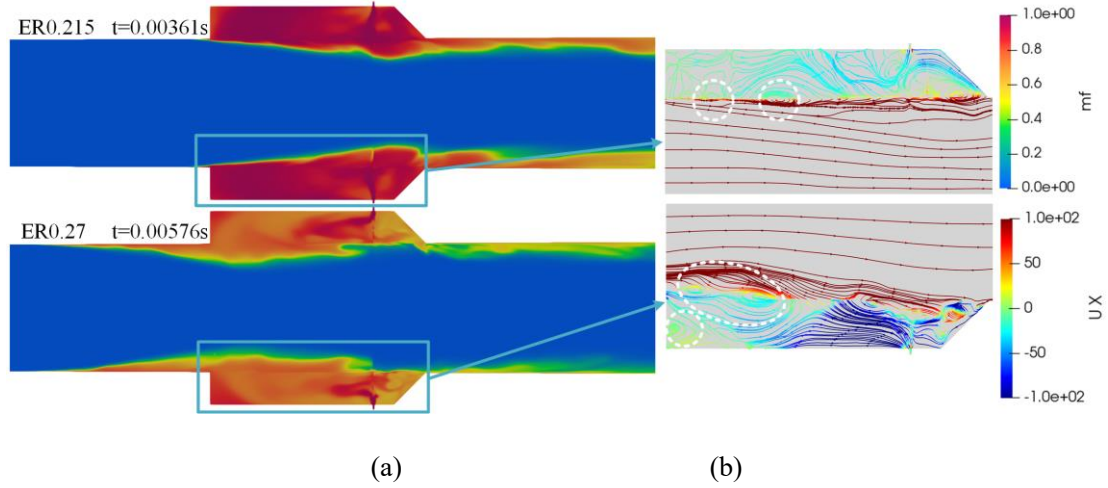


Fig. 19. Mixture fraction and streamwise velocity distributions

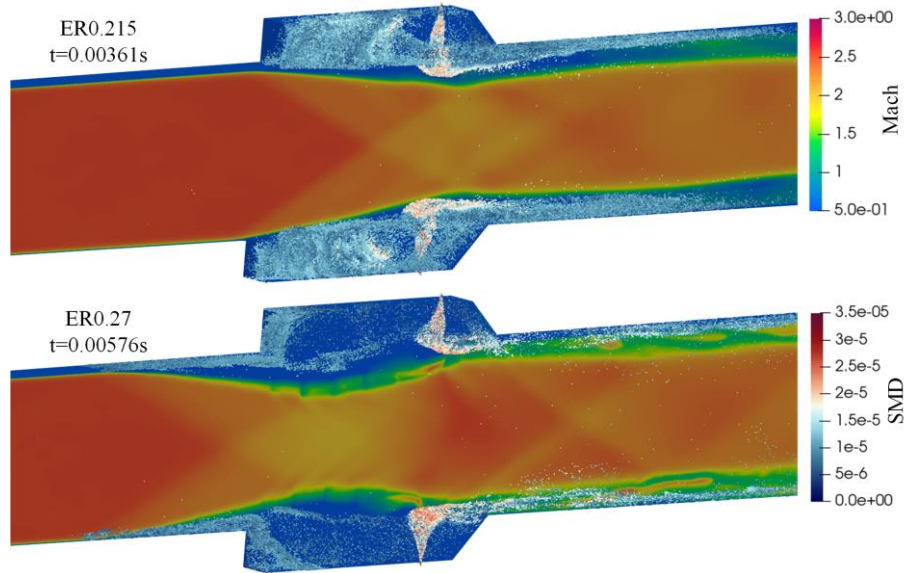


Fig. 20. Mach number and kerosene droplets SMD distribution

As shown in Fig. 21, for low ER, the flame is stabilized in the cavity. However, the kerosene droplets affected by the recirculation-zone 1 continue to propagate downstream along path 5 after path 2 and converge with the kerosene droplets that have just begun to propagate along path 7. Some of the combined kerosene droplets continue to collide with the wall behind the cavity along path 8 while the remaining droplets directly enter the downstream of the cavity along path 11. The combustion process is controlled by the cavity shear layer which can be considered as the cavity shear-layer stabilized combustion.

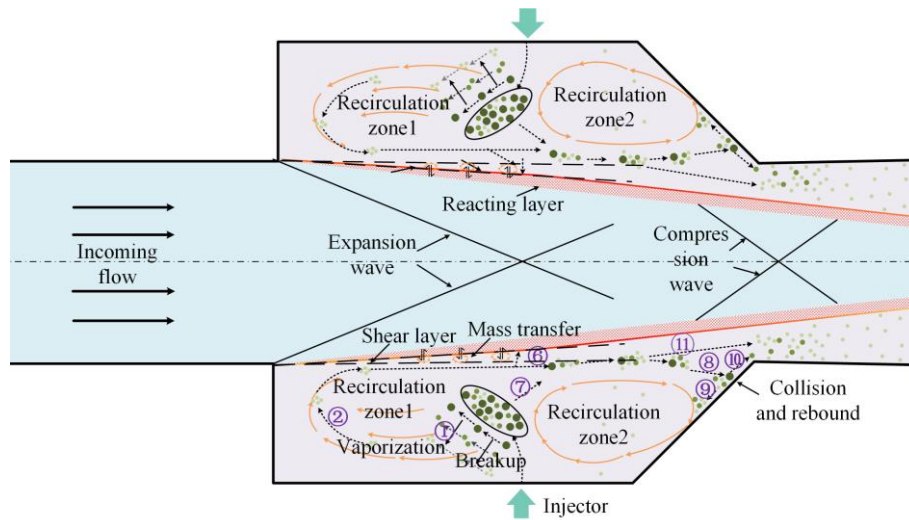


Fig. 21. Kerosene combustion mechanism- liquid kerosene cavity shear-layer stabilized combustion

4. Conclusions

In the process of numerical simulation, gaseous kerosene is often used as a replacement for liquid kerosene. This study focused on analyzing the similarities and differences between gaseous and liquid kerosene properties based on diffusion and combustion characteristics in a cavity-based scramjet combustor using IDDES with the kerosene/air 19 species and 54 reactions mechanism. The combustion processes of gaseous and liquid kerosene were numerically simulated using the same ER, physical model, and numerical method; that is, the SA-based IDDES turbulence model, dynamic zone flamelet model, and 19 species 54 reactions combustion mechanism. The combustion process of liquid kerosene at different ERs was also compared.

The peak pressure of gaseous kerosene combustion near the cavity calculated numerically was significantly lower than the experiment data, while the liquid kerosene combustion exhibited better peak pressure. The injection velocity of gaseous kerosene was an order of magnitude higher than that of liquid kerosene. Liquid kerosene was mixed with the core flow rapidly leaving the cavity, and the residence time of liquid kerosene in the cavity was calculated as two orders of magnitude

higher than that of gaseous kerosene. In addition, the temperature of liquid kerosene in the cavity was much lower than that of gaseous kerosene due to the vaporization of liquid kerosene in the cavity. The high-temperature zone and shock wave predominantly propagated upstream in the combustion process of gaseous kerosene. This indicated that even in skeletal mechanism, the use of gaseous kerosene instead of liquid kerosene combustion will have a large gap in the reaction heat release position.

For the combustion process of liquid kerosene at ER of 0.215, no obvious boundary layer separation in the combustor was observed, flame was stabilized in the cavity, and kerosene droplets gathered in the cavity. The combustion process was controlled by the mixing efficiency of the shear layer and the mode of combustion was identified as cavity shear-layer stabilized combustion. When the values of ER were 0.27 and 0.43, the flame entered the upstream of the cavity and formed boundary layer separation and oblique shock wave. The liquid kerosene droplets were significantly affected by the recirculation-zone 1. The combustion process was controlled by the kerosene transportation of the cavity recirculation zone. This mode of combustion was identified as cavity recirculation-zone stabilized combustion.

Acknowledgments

This research is sponsored by National Natural Science Foundation of China (Grant No. 51876182 and 11972331), Fundamental Research Funds for the Central Universities of China (Grant No. 20720180058).

Data Availability

The data that support the findings of this study are available from the corresponding author upon reasonable request.

References

- [1] Yao W. Kerosene-fueled supersonic combustion modeling based on skeletal mechanisms. *Acta Mechanica Sinica* 2019;35(6):1155-77.
- [2] Kumaran K, Babu V. Mixing and combustion characteristics of kerosene in a model supersonic combustor. *J Propuls Power* 2009;25(3):583-92.
- [3] Bao H, Zhou J, Pan Y. The effect of kerosene injection on ignition probability of local ignition in a scramjet combustor. *Acta Astronaut* 2017;132:54-8.
- [4] Li X, Liu W, Yang L, An B, Pan Y, Zhu J. Experimental investigation on fuel distribution in a scramjet combustor with dual cavity. *J Propuls Power* 2018;34(2):552-6.
- [5] Mingbo S, Hongbo W, Zun C, Jiajian Z. *Unsteady supersonic combustion*. Singapore: Springer Nature Singapore Pte Ltd; 2020.
- [6] Li X, Liu W, Pan Y, Liu S. Investigation on ignition enhancement mechanism in a scramjet combustor with dual cavity. *J Propuls Power* 2016;32(2):439-47.
- [7] Yu G, Li J, Chang X, Chen L, Sung C. Investigation of kerosene combustion characteristics with pilot hydrogen in model supersonic combustors. *J Propuls Power* 2001;17(6):1263-72.
- [8] Tian Y, Le J, Yang S, Zhong F. Investigation of combustion characteristics in a kerosene-fueled supersonic combustor with air throttling. *AIAA J* 2020;1-10.
- [9] Tian Y, Yang S, Le J, Zhong F, Tian X. Investigation of combustion process of a kerosene fueled combustor with air throttling. *Combust Flame* 2017;179:74-85.
- [10] Yao W, Yuan Y, Li X, Wang J, Wu K, Fan X. Comparative study of elliptic and round scramjet combustors fueled by rp-3. *J Propuls Power* 2018;34(3):772-86.
- [11] Zhao D, Gutmark E, de Goey P. A review of cavity-based trapped vortex, ultra-compact, high-g, inter-turbine combustors. *Prog Energy Combust Sci* 2018;66:42-82.
- [12] Chen S, Zhao D. Numerical study of non-reacting flowfields of a swirling trapped vortex ramjet combustor. *Aerosp Sci Technol* 2018;74:81-92.
- [13] Chen S, Zhao D. Numerical study of guide vane effects on reacting flow characteristics in a trapped vortex combustor. *Combustion Science and Technology* 2018;190(12):2111-33.
- [14] Huang Z, He G, Qin F, Xue R, Wei X, Shi L. Combustion oscillation study in a kerosene fueled rocket-based combined-cycle engine combustor. *Acta Astronaut* 2016;129:260-70.
- [15] Li P, Li C, Wang H, Sun M, Liu C, Wang Z, et al. Distribution characteristics and mixing mechanism of a liquid jet injected into a cavity-based supersonic combustor. *Aerosp Sci Technol* 2019;94.
- [16] Choubey G, D Y, Huang W, Yan L, Babazadeh H, Pandey KM. Hydrogen fuel in scramjet engines - a brief review. *Int J Hydrog* 2020;45(33):16799-815.
- [17] Urzay J. Supersonic combustion in air-breathing propulsion systems for hypersonic flight. *Annu Rev Fluid Mech* 2018;50(1):593-627.
- [18] Yao W, Wu K, Fan X. Influences of domain symmetry on supersonic combustion modeling. *J Propuls Power* 2019;35(2):451-65.
- [19] Kumaran K, Behera PR, Babu V. Numerical investigation of the supersonic combustion of kerosene in a strut-based combustor. *J Propuls Power* 2010;26(5):1084-91.
- [20] Liu G, Xu X, Xie Y. Numerical investigation on the supersonic combustion of liquid kerosene in a dual-staged strut based scramjet combustor. *50th AIAA/ASME/SAE/ASEE Joint Propulsion Conference*. 2014.

- 525 [21] Rajasekaran A. SG, Babu V. Numerical simulation of the supersonic combustion of kerosene in
526 a model combustor. *Prog Comput Fluid Dyn* 2009;9:13.
- 527 [22] Li P, Wang H, Sun M, Liu C, Li F. Numerical study on the mixing and evaporation process of a
528 liquid kerosene jet in a scramjet combustor. *Aerosp Sci Technol* 2021;119.
- 529 [23] Hou L, Niu D, Pan P, Ma X, Gang Q. Effects of kerosene global reaction mechanisms on
530 supersonic combustion. *Tuijin Jishu* 2013;34(7):938-43.
- 531 [24] Liu G, Zhu S, Tian L, Luo Yu, Xu X. Numerical investigation of the effect of reaction models
532 on the supersonic combustion of liquid kerosene. *51st AIAA/SAE/ASEE Joint Propulsion
533 Conference*. 2015.
- 534 [25] Yang J, Wu X-y, Wang Z-g. Parametric study of fuel distribution effects on a kerosene-based
535 scramjet combustor. *Int J Aerosp Eng* 2016;2016:1-14.
- 536 [26] Yan Z, Shaohua Z, Bing C, Xu X. Hysteresis of mode transition in a dual-struts based scramjet.
537 *Acta Astronaut* 2016;128:147-59.
- 538 [27] Dharavath M, Manna P, Sinha PK, Chakraborty D. Numerical analysis of a kerosene-fueled
539 scramjet combustor. *J Therm Sci Eng Appl* 2016;8(1).
- 540 [28] Tian Y, Xiao B, Zhang S, Xing J. Experimental and computational study on combustion
541 performance of a kerosene fueled dual-mode scramjet engine. *Aerosp Sci Technol* 2015;46:451-
542 8.
- 543 [29] Clark RJ. Numerical simulation and modeling of combustion in scramjets. *Western Michigan
544 University*. PHD. Western Michigan University; 2015.
- 545 [30] Zettervall N, Fedina E, Nordin-Bates K, Heimdal Nilsson E, Fureby C. Combustion les of a
546 multi-burner annular aeroengine combustor using a skeletal reaction mechanism for jet-a air
547 mixtures. *51st AIAA/SAE/ASEE Joint Propulsion Conference*. 2015.
- 548 [31] Zhang M, Hu Z, Luo KH, He G. Les of kerosene spray combustion with pilot flame in a model
549 dual mode ramjet chamber. *45th AIAA/ASME/SAE/ASEE Joint Propulsion Conference &
550 Exhibit*. 2009.
- 551 [32] Zhang M, Hu Z, He G, Liu P. Large-eddy simulation of kerosene spray combustion in a model
552 scramjet chamber. *Proc Inst Mech Eng G J Aerosp Eng* 2010;224(9):949-60.
- 553 [33] Spalart PR, Allmaras SR. A one-equation turbulence model for aerodynamic flows. *30th
554 Aerospace Sciences Meeting & Exhibit*. 1992.
- 555 [34] Shen W, Huang Y, You Y, Yi L. Characteristics of reaction zone in a dual-mode scramjet
556 combustor during mode transitions. *Aerospace Science and Technology* 2020;99.
- 557 [35] Shur ML, Spalart PR, Strelets MK, Travin AK. A hybrid rans-les approach with delayed-des and
558 wall-modelled les capabilities. *International Journal of Heat and Fluid Flow* 2008;29(6):1638-
559 49.
- 560 [36] Yao W. On the application of dynamic zone flamelet model to large eddy simulation of
561 supersonic hydrogen flame. *Int J Hydrog* 2020;45(41):21940-55.
- 562 [37] Yao W, Wu K, Fan X. Development of skeletal kerosene mechanisms and application to
563 supersonic combustion. *Energy Fuels* 2018;32(12):12992-3003.
- 564 [38] Liu AB, Mather, D., Reitz, R.D. Modeling the effects of drop drag and breakup on fuel sprays.
565 *J Engines* 1993;102:63-95.
- 566 [39] Gosman AD, Ioannides E. Aspects of computer simulation of liquid-fuelled combustors. *AIAA
567 19th Aerospace Sciences Meeting*. Louis, Missouri; 1981.
- 568 [40] Beale JC, .Reitz RD. Modeling spray atomization with the kelvin-helmholtz/rayleigh-taylor

569 hybrid model *At Sprays* 1999;6: 623–50.

570 [41] Zuo B, Gomes, A. M. and Rutland C. J. Studies of superheated fuel spray structures and
571 vaporization in gdi engines. *Int J Engine Res* 2000;1:321-36.

572 [42] Ranz WE, Marshall, W. R. Evaporation from drops part 1. *Chem Eng Prog* 1952;22:141-6.

573 [43] Yao W, Wu K, Fan X. Development of skeletal kerosene mechanisms and application to
574 supersonic combustion. *Energy & Fuels* 2018;32(12):12992–3003.

575 [44] Yao W, Liu H, Li L, Yue L. Nonequilibrium effect modeling in high-ma scramjet based on
576 dynamic zone model. *AIAA Propulsion and Energy 2021 Forum*. AIAA 2021-3543. Virtual
577 Event; 2021.

578 [45] Lee Y, Yao W, Fan X. A low-dissipation solver based on openfoam designed for large eddy
579 simulation in compressible flows. *21st AIAA International Space Planes and Hypersonics
580 Technologies Conference*. AIAA 2017-2444. Xiamen, China; 2017.

581 [46] Vuorinen V, Larmi M, Schlatter P, Fuchs L, Boersma BJ. A low-dissipative, scale-selective
582 discretization scheme for the navier–stokes equations. *Comput fluids* 2012;70:195-205.

583 [47] Segal C. *The scramjet engine processes and characteristics*. Cambridge University Press; 2009.

584 [48] Wang H, Wang Z, Sun M, Wu H. Combustion modes of hydrogen jet combustion in a cavity-
585 based supersonic combustor. *Int J Hydrog Energy* 2013;38(27):12078-89.

586